Using Ricci Flow in the Construction of Homogeneous Cosmological Models

Fan Zhang [a,b] and Lee Lindblom [c]
[a] Institute for Frontiers in Astronomy and Astrophysics, Beijing Normal University, Beijing 102206, China
[b] Gravitational Wave and Cosmology Laboratory, School of Physics and Astronomy, Beijing Normal University, Beijing 100875, China and
[c] Department of Physics, University of California at San Diego, La Jolla, CA 92093, USA
(Dated: October 21, 2026)

This study develops numerical methods for computing homogeneous and isotropic cosmological models on manifolds with non-trivial spatial topologies. The use of Ricci flow is introduced here to aid in the construction of globally homogeneous initial data on these manifolds. The initial data produced in this way are evolved by solving Einstein's equation numerically to construct homogeneous and isotropic cosmological models on three exemplar manifolds in this study: Seifert-Weber space, the lens space $L(5,2)$, and Sixth-Turn space.

arXiv:2610.27340v1 [gr-qc] 19 Oct 2026

I. INTRODUCTION

The topology of our universe is presently unknown. Several attempts to observe topological imprints in the cosmic microwave radiation have been made, but no definitive topology related structure has yet been detected, see Refs. [1, 2]. Theoretical analyses of possible observable topological effects have been limited to simple cases where the structures of those spaces are known analytically, e.g. see Refs. [2–4]. The purpose of this study is to expand the set of computational tools that facilitate the exploration of cosmological models numerically on a much larger collection of manifolds with non-trivial spatial topologies.

The large-scale geometry of our universe is observed to be nearly homogeneous and isotropic, see Refs. [5, 6]. Modern high precision cosmological observations have discovered a few anomalies, like the Hubble tension [7] and the dipole anomaly [8], that are not accounted for in the standard Friedman-Robertson-Walker models. But these anomalies represent relatively small deviations from the standard models, therefore realistic cosmological models on manifolds with any topology must be nearly homogeneous and isotropic. A previous study, Ref. [9], showed that it was not possible to construct homogeneous initial data on many manifolds simply by solving a simple conformal version of the Einstein initial value equations. This study introduces the use of Ricci flow as a tool in the construction of realistic cosmological initial data that can overcome that limitation in many cases. Ricci flow is a parabolic equation for the spatial metric that drives the geometry toward a uniform curvature state, see Refs. [10, 11]. This study demonstrates this use of Ricci flow by constructing homogeneous and isotropic initial data on manifolds with a range of non-trivial topologies.

The numerical methods used in this study are based on a series of papers, Refs. [9, 12–17], that develop methods for solving partial differential equations on manifolds with arbitrary spatial topologies. These methods were created to solve Einstein's evolution equation on manifolds with topology $\mathbb{R}\times\Sigma$. The spacelike surfaces, Σ, are represented in these numerical methods as multi-cube structures that consist of collections of non-overlapping cubic coordinate charts whose faces are identified with the faces of neighboring cubes by a collection of maps, see Ref. [12]. These maps define the topological structure of Σ that determines the continuity of scalar fields across the multi-cube interfaces. The differential structures on these multi-cube representations (i.e. the structures that define the continuity of vectors and tensors across the multi-cube interfaces) are fixed by a $\mathcal{C}^1$ reference metric $\tilde{g}_{ij}$ that is specified as part of the multi-cube structure. Suitable reference metrics have been constructed numerically for the manifolds included in this study using the methods described in Refs. [15, 17]. The numerical methods used in this study have been used previously to solve Einstein's equation on a small collection of manifolds, see Refs. [9, 13, 18]. These numerical methods have also been used to solve the Ricci flow equation on two-dimensional manifolds with non-trivial topologies, see Ref. [14]. Those methods are extended here to provide the numerical solutions to the Ricci flow equation used in the construction of the initial data for Einstein's equation on spatial manifolds, Σ, from a large collection of three-dimensional manifolds.

This study has constructed numerical solutions to the Ricci flow equation, and from them homogeneous and isotropic cosmological models, on three exemplar manifolds: Seifert-Weber space, the lens space $L(5,2)$, and Sixth-Turn space. Seifert-Weber space is constructed topologically by identifying opposite faces of a dodecahedron after twisting the faces by the angle $3\pi/5$, see Ref. [19]. It belongs to the hyperbolic geometry class of manifolds that admit negative scalar curvature geometries. The lens space $L(5,2)$ is constructed by identifying points on the three-sphere S^3 which are related by a discrete isometry specified by the integers p and q. In particular, let the complex numbers (z_1,z_2) represent a point on S^3 as a point on the unit sphere in $\mathbb{C}^2$. The lens space $L(p,q)$ is the quotient space that identifies the point (z_1,z_2) on S^3 with the point $(e^{2\pi i/p}\,z_1, e^{2\pi iq/p}\,z_2)$, see Refs. [20, 21]. These lens spaces belong to the S^3 geometry class of manifolds which admit positive scalar

curvature geometries. The Sixth-Turn space can be constructed topologically by identifying opposite rectangular faces of a hexagonal cylinder, and then identifying the two hexagonal faces after twisting by $2\pi/6$, see Ref. [21]. The Sixth-Turn space (also called $E5$ in some literature, see Ref. [21, 22]) is one of the six compact orientable three-manifolds that admits a global flat metric. The multi-cube structures used in this study for these manifolds are given explicitly as tables in Ref. [15]: Table D.7 for the Seifert-Weber space, Table D.6 for the lens space $L(5,2)$, and Table D.2 for Sixth-Turn space.

This paper is organized as follows: Section II describes the volume preserving form of the three-dimensional Ricci flow equation used in this study. This section also describes a collection of norms used to measure the homogeneity and isotropy of the geometries produced by the Ricci flow evolutions.

Section III describes the numerical Ricci flow evolutions performed for this study on Seifert-Weber space, the lens space $L(5,2)$, and the Sixth-Turn space. These numerical results are shown to be convergent as $N_{\rm grid}$ (the number of grid points in each direction in each multi-cube region) increases. In particular, these results are shown to converge toward homogeneous and isotropic geometries as $N_{\rm grid}$ increases.

Section IV uses the results of these Ricci flow evolutions as the conformal metrics in the solution of the Einstein initial value problem. The initial value problem used here is a particularly simple one in which the cosmological constant is assumed to dominate over the normal matter content of the universe, see Ref. [16].

Section V evolves these initial data using a covariant symmetric-hyperbolic representation of Einstein's equation, which is summarized in some detail in Appendix A. These evolutions are shown to produce spacetimes that converge toward simple homogeneous and isotropic cosmological models. Although expressed in very different coordinates, these numerical cosmological models are shown to have the same expansion histories as the analogous simple Friedman-Robertson-Walker cosmologies.

Finally, Sec. VI summarizes and discusses the new results of this study, describes some limitations to these results, and presents some ideas for future studies.

II. RICCI FLOW: EQUATIONS

This section presents the version of the three-dimensional Ricci flow equation used in this study. This section also describes the numerical method used to enforce the appropriate boundary conditions at the interfaces between multi-cube coordinate patches. Several norms are also defined in this section that can be used to measure the homogeneity and isotropy of the spatial geometries produced by the Ricci flow evolutions.

Ricci flow is a parabolic evolution equation for the spatial metric g_{ij}, which can be written as

$$\partial_t g_{ij} \;=\; F_{ij}, \tag{1}$$

where F_{ij} is given by

$$\begin{aligned} F_{ij} \;=\; & -2R_{ij} + \nabla_i \Delta_j + \nabla_j \Delta_i \\ & + \tfrac{2}{3}\, \langle\!\langle R(t) \rangle\!\rangle\, g_{ij} - \tfrac{2}{3}\, \mu \frac{\mathcal{V}(t) - \mathcal{V}_0}{\mathcal{V}(t)}\, g_{ij}, \end{aligned} \tag{2}$$

see Ref. [10]. The principal terms on the right side of Eq. (2) are the Ricci tensor, R_{ij}, and the terms containing the covector, Δ_i, defined by

$$\Delta_i = g_{ij} g^{k\ell} (\Gamma^j_{k\ell} - \tilde{\Gamma}^j_{k\ell}). \tag{3}$$

The connection $\Gamma^j_{k\ell}$ that appears in Eq. (3), is the Christoffel connection associated with the metric g_{ij}, while $\tilde{\Gamma}^j_{k\ell}$ is any other fixed connection on the manifold. These "DeTurck" terms (those containing Δ_i) are added to make Eq. (1) strongly parabolic, and thus to have a well-posed initial value problem, see Refs. [23, 24].

The terms in Eq. (2) containing the spatially averaged Ricci scalar curvature, $\langle\!\langle R \rangle\!\rangle$,

$$\langle\!\langle R \rangle\!\rangle = \frac{\int R \sqrt{g}\, d^3x}{\mathcal{V}}, \tag{4}$$

and the spatial volume $\mathcal{V}$,

$$\mathcal{V} = \int \sqrt{g}\, d^3x. \tag{5}$$

have been added to Eq. (1) to control the evolution of the volume of the manifold. Contracting Eq. (1) with the inverse metric g^{ij} and integrating the result over any compact manifold without boundary provides the following evolution equation for the volume $\mathcal{V}(t)$ of that manifold:

$$\partial_t \left[\mathcal{V}(t) - \mathcal{V}_0 \right] = -\mu \left[\mathcal{V}(t) - \mathcal{V}_0 \right]. \tag{6}$$

Without the term proportional to μ, the volume of the manifold would be fixed, $\partial_t \mathcal{V}(t) = 0$, at the analytical level. In numerical simulations, however, discretization and roundoff error give rise to slow, approximately linear drifts in the volume. With the damping term, however, the volume of the manifold is driven toward the target value $\mathcal{V}_0$ at a rate determined by the constant μ. The numerical value $\mu = 10$ was found to be useful in the evolutions for this study.

Penalty terms have been added to the Ricci flow equations at the boundaries between multi-cube regions to ensure the metric and its derivatives are continuous across those boundaries. At these boundary interface points the standard Ricci flow equation, Eq. (1), is replaced with

$$\begin{aligned} \partial_t g_{ij} \;=\; & F_{ij} - \alpha \Big(g_{ij} - \langle g_{ij} \rangle \Big) \\ & - \beta \left(\tilde{n}^k \tilde{\nabla}_k\, g_{ij} + \Big\langle \tilde{n}^k \tilde{\nabla}_k\, g_{ij} \Big\rangle \right). \end{aligned} \tag{7}$$

The vector $\tilde{n}^k$ is the unit normal to the boundary surface using the reference metric $\tilde{g}_{ij}$ that defines the differential structure of the manifold: $\tilde{n}^m \tilde{n}^n\, \tilde{g}_{mn} = 1$. The

tensor $\tilde{n}^k \tilde{\nabla}_k g_{ij}$ is the normal component of the torsion-free reference-metric compatible covariant derivative of g_{ij}:

$$\tilde{n}^k \tilde{\nabla}_k g_{ij} = \tilde{n}^k \partial_k g_{ij} - \tilde{n}^k \tilde{\Gamma}^l_{ki}\, g_{lj} - \tilde{n}^k \tilde{\Gamma}^l_{kj}\, g_{il}. \quad (8)$$

The expressions $\langle g_{ij} \rangle$ and $\langle \tilde{n}^k \tilde{\nabla}_k g_{ij} \rangle$ represent the values of those tensors on the boundaries of the neighboring multi-cube region that have been transformed into the local coordinate basis using the boundary interface maps (see Ref. [13] for details). The constants α and β determine the sizes of these penalty terms. The values of these constants used in the evolutions for this study are

$$\alpha = N^2_{\rm grid}, \quad (9)$$
$$\beta = 1, \quad (10)$$

where $N_{\rm grid}$ is the number of grid points in the normal direction of the particular region. These values of α and β ensure the boundary conditions $g_{ij} = \langle g_{ij} \rangle$ and $\tilde{n}^k \tilde{\nabla}_k g_{ij} = \langle \tilde{n}^k \tilde{\nabla}_k g_{ij} \rangle$ are accurately enforced without making the evolution numerically unstable. Equation (7) therefore enforces continuity across the boundary of both the metric and its normal derivatives.

Several norms have been introduced to measure how well the numerical Ricci flow evolutions are driven toward a homogeneous and isotropic state. The first norm measures the spatial variations in the Ricci scalar curvature, R. The average value of these spatial variations is given by $\langle\!\langle \Delta R \rangle\!\rangle$, defined by

$$\langle\!\langle \Delta R \rangle\!\rangle^2 = \frac{1}{\mathcal{V}} \int \left(R - \langle\!\langle R \rangle\!\rangle\right)^2 \sqrt{g}\, d^3x. \quad (11)$$

A dimensionless norm, $\| \Delta R \|$, defined by

$$\| \Delta R \| = \frac{\langle\!\langle \Delta R \rangle\!\rangle}{|\langle\!\langle R \rangle\!\rangle|}, \quad (12)$$

can also be useful except in cases where $\langle\!\langle R \rangle\!\rangle \approx 0$.

The homogeneity of the full spatial Ricci tensor can be explored further using the curvature scalar $\mathscr{R}$ defined by

$$\mathscr{R}^2 = 3 R_{ij} R^{ij}. \quad (13)$$

Its spatial average $\langle\!\langle \mathscr{R} \rangle\!\rangle$ is defined by

$$\langle\!\langle \mathscr{R} \rangle\!\rangle = \frac{1}{\mathcal{V}} \int \mathscr{R} \sqrt{g}\, d^3x, \quad (14)$$

and its average spatial variations $\langle\!\langle \Delta \mathscr{R} \rangle\!\rangle$ are given by,

$$\langle\!\langle \Delta \mathscr{R} \rangle\!\rangle^2 = \frac{1}{\mathcal{V}} \int \left(\mathscr{R} - \langle\!\langle \mathscr{R} \rangle\!\rangle\right)^2 \sqrt{g}\, d^3x. \quad (15)$$

A dimensionless norm $\| \Delta \mathscr{R} \|$ defined by

$$\| \Delta \mathscr{R} \| = \frac{\langle\!\langle \Delta \mathscr{R} \rangle\!\rangle}{\langle\!\langle \mathscr{R} \rangle\!\rangle}, \quad (16)$$

can also be useful except in cases where $\langle\!\langle \mathscr{R} \rangle\!\rangle \approx 0$.

If the Ricci tensor is determined completely by the Ricci scalar, $R_{ij} = \frac{1}{3} g_{ij} R$, then its eigenvalues are identical and the geometry is isotropic. In this case the curvature scalar $\mathscr{R}$ equals the Ricci scalar: $\mathscr{R}^2 = R^2$. Conversely if $\mathscr{R}^2 = R^2$ then the spatial geometry must be isotropic. Consider a frame in which the Ricci tensor is diagonal, with eigenvalues R_1, R_2 and R_3. The Ricci scalar R is given in this case by $R = R_1 + R_2 + R_3$, while the curvature scalar $\mathscr{R}$ is given by $\mathscr{R}^2 = 3(R_1^2 + R_2^2 + R_3^2)$. Using these expressions it follows that

$$\mathscr{R}^2 - R^2 = (R_1 - R_2)^2 + (R_1 - R_3)^2 + (R_2 - R_3)^2. \quad (17)$$

Therefore, if $\mathscr{R}^2 = R^2$ then $R_1 = R_2 = R_3$, so the geometry is isotropic. One practical measure of the isotropy of the geometry is given by the quantity $\langle\!\langle \mathscr{I} \rangle\!\rangle$ defined by

$$\langle\!\langle \mathscr{I} \rangle\!\rangle = \big| |\langle\!\langle R \rangle\!\rangle| - \langle\!\langle \mathscr{R} \rangle\!\rangle \big|. \quad (18)$$

The dimensionless norm $\| \mathscr{I} \|$ defined by

$$\| \mathscr{I} \| = \frac{\langle\!\langle \mathscr{I} \rangle\!\rangle}{|\langle\!\langle R \rangle\!\rangle|}, \quad (19)$$

can also be useful except in cases where $\langle\!\langle R \rangle\!\rangle \approx 0$.

III. RICCI FLOW: NUMERICAL RESULTS

This section describes the numerical methods used in this study to solve the Ricci flow equation on three-dimensional manifolds with non-trivial topologies. The geometries produced by these Ricci flow solutions will be shown to be homogeneous and isotropic. These geometries do not satisfy Einstein's equation, but they can be used to construct simple homogeneous and isotropic cosmological models that do satisfy Einstein's equation in Secs. IV and V.

The volume-normalized Ricci flow equation with DeTurck gauge fixing, Eq. (1), has been implemented for this study in the `SpEC` numerical relativity code (developed originally by the Caltech and Cornell numerical relativity groups). This code evolves PDEs using pseudo-spectral methods to evaluate spatial derivatives, and performs explicit time integration at each grid point using standard ordinary differential equation solvers (e.g., the Dormand-Prince, Refs. [25, 26], solver used in this study). The Ricci flow equation is parabolic and has been implemented in `SpEC` as a FOTSOS (First-Order-Time-Second-Order-Space) evolution system. Boundary conditions are imposed at multi-cube interface boundaries to enforce continuity of the metric g_{ij} and the normal covariant derivative $\tilde{n}^k \tilde{\nabla}_k g_{ij}$ using penalty methods as described in Sec. II, and in more detail in Ref. [15]. In this study the reference connection $\tilde{\Gamma}^k_{ij}$ that appears in the DeTurck terms of the Ricci flow Eq. (1) is the one associated with the reference metric $\tilde{g}_{ij}$ constructed numerically for each

manifold using the methods described in Ref. [15].[1]

The Ricci flow equation on Seifert-Weber space has been solved for this study using the reference metric $\tilde{g}_{ij}$ as initial conditions. These evolutions have been carried out using multi-cube structures with a range of different $N_{\rm grid}$ grid points in each spatial direction, $N_{\rm grid} = \{16, 20, 24, 28\}$, so that the numerical convergence of the results can be assessed. Figure 1 illustrates the evolutions of the spatial variations in the Ricci scalar, $\| \Delta R \|$, defined in Eq. (12). Figure 2 illustrates the evolution of the spatial variations in the curvature scalar, $\| \Delta \mathscr{R} \|$, defined in Eq. (16). And Fig. 3 illustrates the evolution of the isotropy norm, $\| \mathscr{I} \|$ defined in Eq. (19). These figures demonstrate that the Ricci flow evolutions on the Seifert-Weber manifold are convergent and that they drive the metric toward a homogeneous and isotropic state.

The Ricci flow equation is a parabolic system of equations for the metric g_{ij}. The numerical evolution of parabolic equations is very inefficient because the maximum time step allowed for numerical stability is extremely short, see Refs. [27, 28]. Consequently these Ricci flow evolutions take a lot of computational resources. For example, the evolutions on Seifert-Weber space took a total of 10,267 cpu hours, or 513 cpu hours for each of the 20 cubic regions used to represent this space. In order to improve the efficiency of these computations a bootstrap method was developed for the Ricci flow evolutions on the lens space $L(5, 2)$, and the Sixth-Turn space. In this method the lowest resolution, $N_{\rm grid} = 16$, evolution is performed using the reference

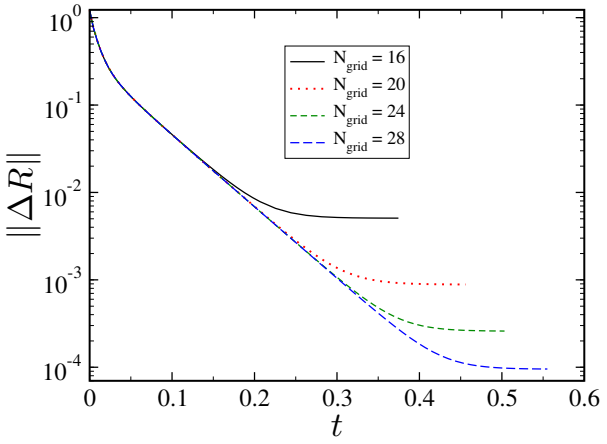


FIG. 1: This figure illustrates the norm $\| \Delta R \|$ defined in Eq. (12) that measures the average spatial variations of the Ricci scalar R for the Ricci flow evolutions on the Seifert-Weber manifold.

[1] Reference metrics were constructed on each multi-cube manifold by first constructing flat metrics in the neighborhood of each multi-cube vertex, then combining those flat metrics with a partition of unity to form a global $\mathcal{C}^0$ metric, and finally smoothing those global $\mathcal{C}^0$ metrics across each interface between cubic regions to create a global $\mathcal{C}^1$ metric by solving a sequence of differential equations numerically.

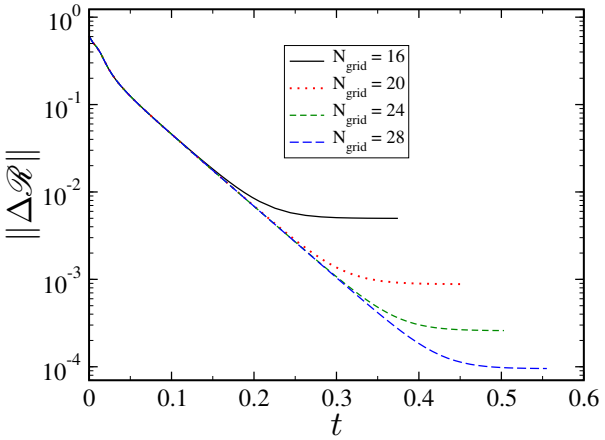


FIG. 2: This figure illustrates the norm $\| \Delta \mathscr{R} \|$ defined in Eq. (16) that measures the average spatial variations of the curvature scalar $\mathscr{R}$ for the Ricci flow evolutions on the Seifert-Weber manifold.

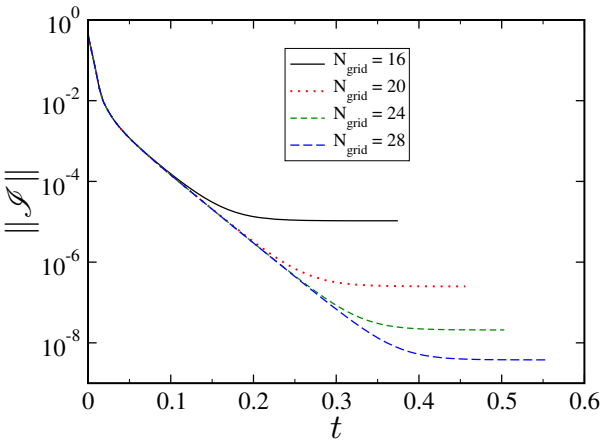


FIG. 3: This figure illustrates the norm $\| \mathscr{I} \|$ defined in Eq. (19) that measures the fractional differences between the Ricci scalar norm $\langle\!\langle R \rangle\!\rangle$ and the curvature scalar norm $\langle\!\langle \mathscr{R} \rangle\!\rangle$ for the Ricci flow evolutions on the Seifert-Weber manifold. The equality $\mathscr{R}^2 = R^2$ implies the isotropy of the spatial geometry.

metric $\tilde{g}_{ij}$ for that manifold as initial data. This lowest resolution evolution is continued until $\langle\!\langle \Delta R \rangle\!\rangle$, the spatial variations in the Ricci scalar curvature defined in Eq. (11), becomes constant (as seen for example in Fig. 1 for the Seifert-Weber evolutions). The metric g_{ij} that results from this initial evolution is then interpolated onto the next higher resolution grid, $N_{\rm grid} = 20$. These higher resolution data are used as initial data for the next Ricci flow evolution which is continued until $\langle\!\langle \Delta R \rangle\!\rangle$ again becomes constant. This bootstrap process is repeated iteratively to produce the $N_{\rm grid} = \{20, 24, 28\}$ resolution solutions to the Ricci flow equations on the lens space $L(5, 2)$ and on Sixth-Turn space. Using this bootstrap procedure reduces the total computational time by about a factor of five: taking 101 cpu hours for each cubic region on the lens space $L(5, 2)$, and 107 cpu hours per cubic region on Sixth-Turn space.

Solving the Ricci flow equations on a sequence of grids

with different resolutions using this bootstrap method does not produce complete evolution plots comparable to those in Figs. 1–3 for the Seifert-Weber case. The final Ricci flow metrics produced by this process can, however, be determined and from them the numerical convergence of the spatial variations in their curvature scalars, $\langle\!\langle\, \Delta R \,\rangle\!\rangle$ and $\langle\!\langle\, \Delta\mathscr{R} \,\rangle\!\rangle$, as well as the isotropy parameter $\langle\!\langle\, \mathscr{I} \,\rangle\!\rangle$ can be evaluated. Figures 4–6 compare these convergence results for the Seifert-Weber, the lens space $L(5,2)$, and Sixth-Turn space. These results show that the Ricci flow evolutions are convergent toward geometries that are spatially homogeneous and isotropic on these manifolds.

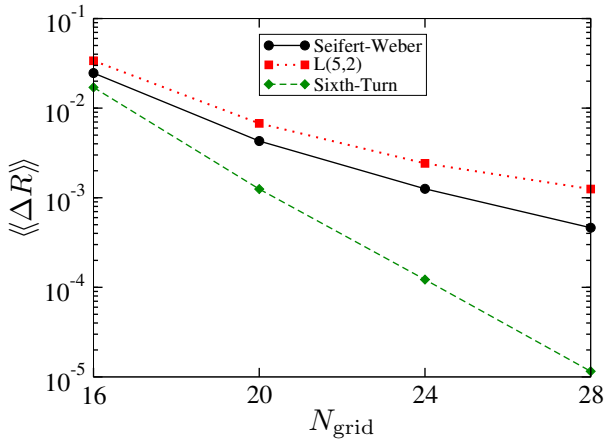


FIG. 4: This figure illustrates the convergence of $\langle\!\langle\, \Delta R \,\rangle\!\rangle$ defined in Eq. (11) as functions of the grid spacing parameter $N_{\rm grid}$ for the Ricci flow evolutions on the Seifert-Weber, L(5,2), and Sixth-Turn manifolds.

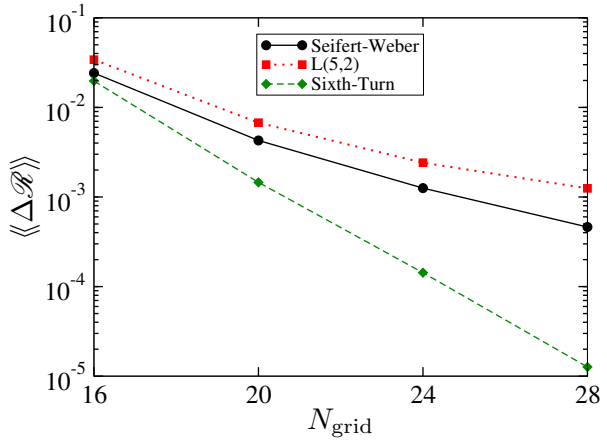


FIG. 5: This figure illustrates the convergence of $\langle\!\langle\, \Delta\mathscr{R} \,\rangle\!\rangle$ defined in Eq. (15) as functions of the grid spacing parameter $N_{\rm grid}$ for the Ricci flow evolutions on the Seifert-Weber, L(5,2), and Sixth-Turn manifolds.

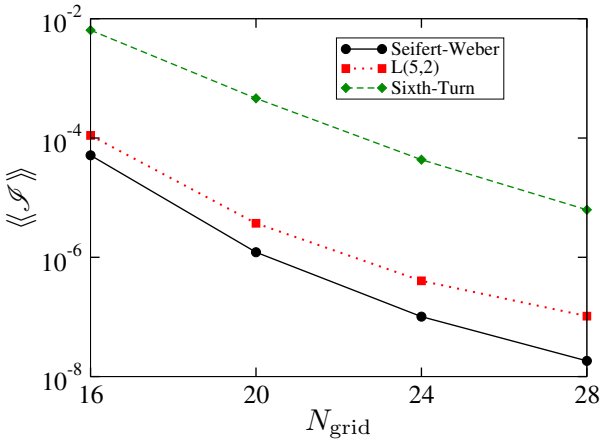


FIG. 6: This figure illustrates the convergence of $\langle\!\langle\, \mathscr{I} \,\rangle\!\rangle$ defined in Eq. (18) as functions of the grid spacing parameter $N_{\rm grid}$ for the Ricci flow evolutions on the Seifert-Weber, L(5,2), and Sixth-Turn manifolds.

IV. SIMPLE INITIAL DATA

This section describes the method used in this study to find solutions to the Einstein initial value equations. The goal is to construct initial data that can be used to evolve simple homogeneous cosmological models on these manifolds. The Einstein constraint equations determine the allowed initial data for the spatial metric g_{ij} and extrinsic curvature K_{ij} on a spacelike hypersurface. The simplest solutions to these equations are determined by specifying a conformal metric, $\tilde{g}_{ij}$, and a constant, K, that functions as the trace of the extrinsic curvature. The physical metric g_{ij} and the full extrinsic curvature K_{ij} in this approach are given by

$$g_{ij} = \phi^4 \tilde{g}_{ij}, \tag{20}$$

$$K_{ij} = \tfrac{1}{3}\phi^4 \tilde{g}_{ij} K, \tag{21}$$

where ϕ is a conformal factor. This conformal factor is determined by solving the constraint equations, which for this simple case reduce to a second-order elliptic partial differential equation for ϕ.

The methods for solving the particular version of the Einstein constraint equations used in this study were developed in Ref. [16] for manifolds with non-trivial topologies. This form of the initial value problem assumes that the average matter content in these solutions is negligible compared to the cosmological constant Λ. With this assumption the Einstein constraint equation reduces to

$$\tilde{\nabla}^i \tilde{\nabla}_i \phi = \tfrac{1}{8}\phi \tilde{R} + \tfrac{1}{12}\phi^5 (K^2 - 3\Lambda), \tag{22}$$

where $\tilde{\nabla}_i$ and $\tilde{R}$ are the covariant derivative and Ricci scalar curvature respectively associated with the conformal metric $\tilde{g}_{ij}$. The conformal metrics $\tilde{g}_{ij}$ used in this study are the solutions to the Ricci flow equation described in Sec. III.

The integral of the left side of Eq. (22) vanishes on any compact manifold without boundary. Therefore the constants K and Λ must be chosen in a way that makes it possible for the integral of the right side of this equation to vanish as well. Convenient choices for these constants produce solutions to Eq. (22) with $\phi \approx 1$. An acceptable choice can be identified by setting $\phi = 1$ in the expression on the right side of Eq. (22) and integrating over the manifold. Setting this integral to zero results in the following constraint on the values of K and Λ,

$$K^2 - 3\Lambda = -\tfrac{3}{2}\langle\!\langle \tilde{R} \rangle\!\rangle, \tag{23}$$

where $\langle\!\langle \tilde{R} \rangle\!\rangle$ is the average value of the conformal scalar curvature $\tilde{R}$,

$$\langle\!\langle \tilde{R} \rangle\!\rangle = \frac{\int \sqrt{\tilde{g}}\, \tilde{R}\, d^3x}{\int \sqrt{\tilde{g}}\, d^3x}, \tag{24}$$

where $\tilde{g}$ represents the determinant of the conformal metric $\tilde{g}_{ij}$. This choice transforms Eq. (22) into the form

$$\tilde{\nabla}^i \tilde{\nabla}_i \phi \;=\; \tfrac{1}{8}\phi \left(\tilde{R} - \phi^4 \langle\!\langle \tilde{R} \rangle\!\rangle \right). \tag{25}$$

This equation has the exact solution $\phi = 1$ in the constant scalar curvature case $\tilde{R} = \langle\!\langle \tilde{R} \rangle\!\rangle$.

The Ricci scalar curvature R determined from the physical metric g_{ij} is related to the Ricci scalar curvature $\tilde{R}$ associated with the conformal metric $\tilde{g}_{ij}$ by the expression

$$R \;=\; \phi^{-4}\, \tilde{R} - 8\phi^{-5}\, \tilde{\nabla}^i \tilde{\nabla}_i \phi. \tag{26}$$

The Hamiltonian constraint, $\mathcal{H}$, for the initial value problem considered here is given by the expression

$$\mathcal{H} = R + \tfrac{2}{3}\left(K^2 - 3\Lambda\right) = R - \langle\!\langle \tilde{R} \rangle\!\rangle, \tag{27}$$

(see Ref. [16]). Solutions to the Einstein constraint Eq. (25) therefore have physical Ricci scalar curvatures given by

$$R \;=\; \langle\!\langle \tilde{R} \rangle\!\rangle. \tag{28}$$

The accuracy of numerically determined solutions to the initial value problem can be evaluated using the Hamiltonian constraint norm $\| \mathcal{H} \|$ defined by,

$$\| \mathcal{H} \|^2 = \mathcal{V}^{-1} \int \left(R - \langle\!\langle \tilde{R} \rangle\!\rangle \right)^2 \sqrt{g}\, d^3x. \tag{29}$$

The conformal metrics $\tilde{g}_{ij}$ used to solve the initial value problem for this study are the metrics constructed in Sec. III by solving the Ricci flow equation. These Ricci flow metrics have the property that the spatial variations in the Ricci scalar, $\langle\!\langle\, \Delta R \,\rangle\!\rangle$, are very small, see Fig. 4. The Hamiltonian constraint norm $\|\mathcal{H}\|$ is identical to the spatial variations of the Ricci scalar curvature defined in Eq. (11): $\| \mathcal{H} \| = \langle\!\langle\, \Delta R \,\rangle\!\rangle$. Therefore the Ricci flow metrics are themselves solutions to the initial value Eq. (22) with $\phi = 1$. Table I lists the average values of the physical Ricci scalar curvature, $\langle\!\langle R \rangle\!\rangle$, the physical volume $\mathcal{V}$, and the cosmological constant Λ for the initial spatial geometries constructed for each of the manifolds included in this study. The volumes $\mathcal{V}$ measure the physical "sizes" of the manifolds in the length-scale units of our code, and can therefore be used to calibrate the sizes of the curvatures of the geometries. The graphs in Figs. 4 and 5 show that these Ricci flow geometries are homogeneous, and the graph in Fig. 6 shows that they are also isotropic.

TABLE I: Physical properties of the initial data for the manifolds included in this study: the average scalar curvature $\langle\!\langle R \rangle\!\rangle$ defined in Eq. (4), the physical volume $\mathcal{V}$ defined in Eq. (5), and the cosmological constant Λ determined by Eq. (23) for the geometries with $K = -1$ constructed on each manifold.

Manifold	$\langle\!\langle R \rangle\!\rangle$	$\mathcal{V}$	Λ
Seifert-Weber	-4.8467	15.4254	-2.0900
$L(5,2)$	3.9873	7.2874	2.3270
Sixth-Turn	-1.7538×10^{-8}	6.2804	0.3333

V. SIMPLE COSMOLOGICAL MODELS

This section describes the methods used in this study to construct simple homogeneous cosmological models by solving the Einstein evolution equations using the initial data prepared in Secs. III and IV. The spatial metrics, g^0_{ij}, produced by those solutions to the Einstein constraint equations are used in two ways. First, they are used to construct the initial data for the spacetime metric ψ^0_{ab}:

$$ds^2 = \psi^0_{ab}\, dx^a dx^b = -dt^2 + g^0_{ij}\, dx^i dx^j, \tag{30}$$

where the indices from the first part of the alphabet, e.g. a, b, c, ..., range over the four-dimensional spacetime coordinates, while the indices from the later parts of the alphabet, e.g. i, j, k, ..., range over the three-dimensional spatial coordinates on each t = constant hypersurface. Second, the metric ψ^0_{ab} is also used to define the time-independent spacetime reference metric, $\tilde{\psi}_{ab} \equiv \psi^0_{ab}$ that defines the differential structure in these four-dimensional manifolds.

The representation of the Einstein equation used to perform the numerical evolutions in this study is the covariant first-order symmetric-hyperbolic representation developed in Ref. [13]. The dynamical fields in this representation are the spacetime metric, ψ_{ab}, its time derivative, $\Pi_{ab} = -t^c \tilde{\nabla}_c \psi_{ab}$, and its spatial derivatives $\Phi_{iab} = \tilde{\nabla}_i \psi_{ab}$, where t^c is the future directed timelike unit normal ($t^a t^b \psi_{ab} = -1$) to the t = constant hypersurfaces. The derivative, $\tilde{\nabla}_a$, used in these definitions is the torsion-free covariant derivative compatible with the reference metric: $\tilde{\nabla}_c \tilde{\psi}_{ab} = 0$. The basic structure of this

representation of Einstein's equation is summarized more completely in Appendix A. The values of the dynamical fields on the initial spacelike hypersurface used to start the evolutions in this study are given by,

$$\psi^0_{ab} = \tilde{\psi}_{ab}, \quad (31)$$
$$\Pi^0_{tt} = -2K^0, \quad (32)$$
$$\Pi^0_{tk} = 0, \quad (33)$$
$$\Pi^0_{ij} = \tfrac{2}{3}K^0 g^0_{ij}, \quad (34)$$
$$\Phi^0_{iab} = 0, \quad (35)$$

where K^0 is the trace of the extrinsic curvature used to compute the initial data in Sec. IV.

The first-order symmetric-hyperbolic representation of the Einstein system has a large number of constraints, which are described in some detail in Appendix A. The overall magnitude of these constraints is summarized by a quantity $\mathcal{C}_\psi$ defined in Eq. (A.12). The dimensionless norm $\| \mathcal{C}_\psi \|$ defined in Eq. (A.13) provides a useful measure of the fractional constraint violation errors in these cosmological models. Figure 7 illustrates $\| \mathcal{C}_\psi(t) \|$ for the numerical evolutions at each of the numerical resolutions $N_{\rm grid} = \{16, 20, 24, 28\}$ on Seifert-Weber space. This figure shows that these numerical evolutions are convergent solutions to Einstein's equation. Figures 8 and 9 give the analogous results for the lens space $L(5,2)$ and for Sixth-Turn space, demonstrating that these evolutions have produced numerically convergent cosmological models as well.

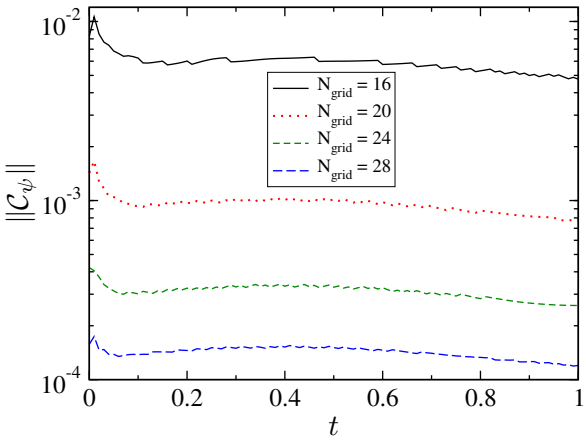


FIG. 7: This figure illustrates the dimensionless constraint norm $\| \mathcal{C}_\psi \|$ defined in Eq. (A.13) that measures the constraint violations for the solutions to the Einstein evolution equations on the Seifert-Weber manifold.

The properties of the cosmological models resulting from the numerical evolutions performed for this study are most easily analyzed by expressing the resulting spacetime metric, ψ_{ab}, in the three-plus-one ADM form (see Ref. [29]):

$$ds^2 = \psi_{ab}\, dx^a dx^b = -N^2 dt^2 + g_{ij}(dx^i + N^i dt)(dx^j + N^j dt), \quad (36)$$

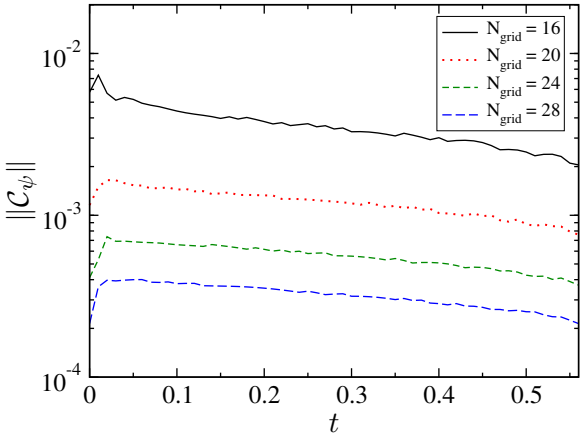


FIG. 8: This figure illustrates the dimensionless constraint norm $\| \mathcal{C}_\psi \|$ defined in Eq. (A.13) that measures the constraint violations for the solutions to the Einstein evolution equations on the $L(5,2)$ manifold.

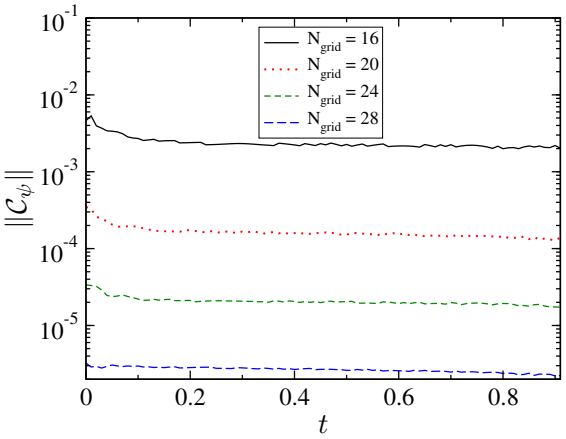


FIG. 9: This figure illustrates the dimensionless constraint norm $\| \mathcal{C}_\psi \|$ defined in Eq. (A.13) that measures the constraint violations for the solutions to the Einstein evolution equations on the Sixth-Turn space.

where N is the lapse, N^i the shift, and g_{ij} the spatial metric on each t = constant hypersurface. The initial data for these cosmological models are evolved numerically until the volumes of the t = constant hypersurfaces increase by about a factor of ten in the lens space $L(5,2)$ and in the Sixth-Turn space cases. The volume in Seifert-Weber space increases initially in these numerical evolutions, but then contracts after reaching a maximum before expanding by a factor of ten. The evolution in this Seifert-Weber case was continued for approximately the same length of coordinate time as the other two cases. Figure 10 illustrates $\mathcal{V}(t)$ for the highest resolution evolutions, $N_{\rm grid} = 28$, on these manifolds.

The homogeneity and isotropy of the geometries of the t = constant hypersurfaces in these simple cosmological models have been evaluated by monitoring the norms $\langle\!\langle\, \Delta R(t)\, \rangle\!\rangle$, $\langle\!\langle\, \Delta \mathscr{R}(t)\, \rangle\!\rangle$, and $\langle\!\langle\, \mathscr{I}(t)\, \rangle\!\rangle$ defined in Eqs. (11), (15) and (18). These quantities were found to be con-

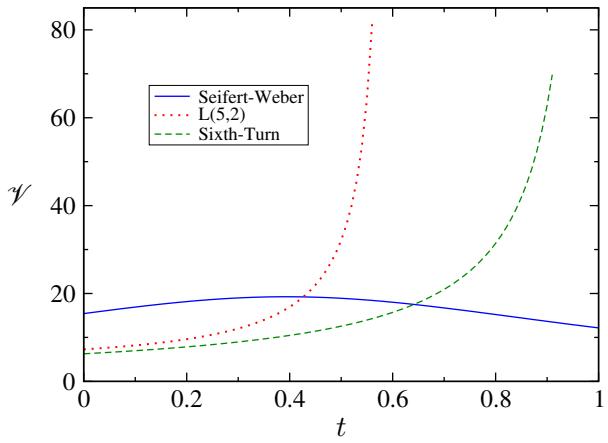


FIG. 10: This figure illustrates the evolution of the volume $\mathscr{V}(t)$ defined in Eq. (5) for the $N_{\rm grid} = 28$ solutions to Einstein's evolution equation on the Seifert-Weber, $L(5,2)$ and the Sixth-Turn manifolds.

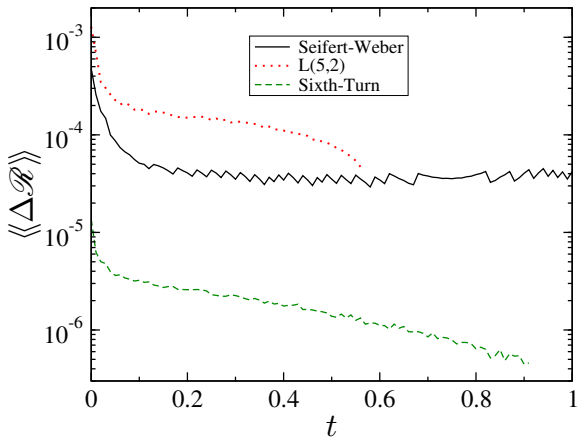


FIG. 12: This figure illustrates the evolution of the norm $\langle\!\langle\, \Delta\mathscr{R}(t)\,\rangle\!\rangle$ defined in Eq. (15) that measures the spatial variations in the curvature scalar $\mathscr{R}$ for the $N_{\rm grid} = 28$ solutions to the Einstein evolution equations on the Seifert-Weber, $L(5,2)$, and the Sixth-Turn manifolds.

vergent as $N_{\rm grid}$ increases for the evolutions on all three manifolds: Seifert-Weber space, the lens space $L(5,2)$, and Sixth-Turn space. In order to reduce the number of graphs, only the highest resolution ($N_{\rm graph} = 28$) results for $\langle\!\langle\, \Delta R(t)\,\rangle\!\rangle$, $\langle\!\langle\, \Delta\mathscr{R}(t)\,\rangle\!\rangle$, and $\langle\!\langle\, \mathscr{I}(t)\,\rangle\!\rangle$ are shown in Figs. 11–13. These graphs show that the homogeneity and the isotropy of these simple cosmological models improve as the geometries expand.

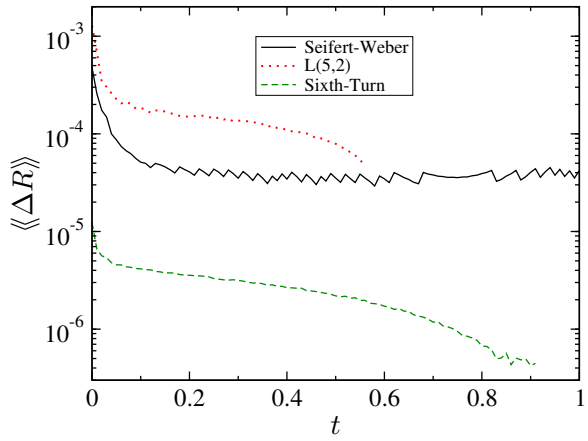


FIG. 11: This figure illustrates the evolution of the norm $\langle\!\langle\, \Delta R(t)\,\rangle\!\rangle$ defined in Eq. (11) that measures the spatial variations in the Ricci scalar curvature R for the $N_{\rm grid} = 28$ solutions to the Einstein evolution equations on the Seifert-Weber, $L(5,2)$, and the Sixth-Turn manifolds.

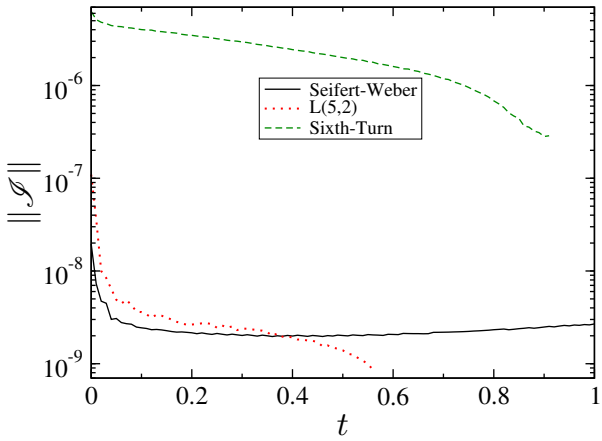


FIG. 13: This figure illustrates the evolution of the norm $\langle\!\langle\, \mathscr{I}(t)\,\rangle\!\rangle$ defined in Eq. (18) that measures the isotropy of the spatial geometry for the $N_{\rm grid} = 28$ solutions to the Einstein evolution equations on the Seifert-Weber, $L(5,2)$, and the Sixth-Turn manifolds.

An important goal of this study is to compare the simple homogeneous and isotropic cosmological models constructed here with the standard Friedman-Robertson-Walker (FRW) cosmological models. The spacetime metric for the FRW cosmological models can be written in the form,

$$ds^2 = -d\eta^2 + a^2(\eta)L^2\left[d\chi^2 + \Xi^2(\chi)\left(d\theta^2 + \sin^2\theta d\varphi^2\right)\right], \tag{37}$$

where $a(\eta)$ is a dimensionless scale factor, L is a characteristic length scale, and $\Xi(\chi)$ is given by

$$\Xi(\chi) = \begin{cases} \sin\chi, & \text{for } k = +1, \\ \chi, & \text{for } k = 0, \\ \sinh\chi, & \text{for } k = -1, \end{cases} \tag{38}$$

for the manifolds with positive, zero, and negative spatial curvatures respectively. The Einstein equations for these

geometries are given by

$$\left(\frac{da}{d\eta}\right)^2 = -\frac{k}{L^2} + \frac{\Lambda}{3}\,a^2, \tag{39}$$

$$\frac{d^2a}{d\eta^2} = \frac{\Lambda}{3}\,a, \tag{40}$$

in a spacetime where the cosmological constant Λ dominates over the matter content of the universe.

There is no *a priori* relationship between the $t =$ constant hypersurfaces produced by the numerical evolutions in this study, and the $\eta =$ constant hypersurfaces used in the descriptions of the simple FRW cosmological models. The $\eta =$ constant hypersurfaces are defined by the homogeneity and isotropy of the spatial geometries in those simple models. The evolution of the $t =$ constant hypersurfaces is determined by the gauge conditions used to perform these numerical evolutions. Figures 11 and 12 show that the $t =$ constant hypersurfaces in the numerical evolutions have curvature scalars R and $\mathscr{R}$ that are essentially constant on those surfaces. Figure 13 shows these geometries are also essentially isotropic on those surfaces. Therefore the $t =$ constant hypersurfaces of the numerical evolutions coincide (within the accuracy of the numerical evolutions) with the $\eta =$ constant hypersurfaces of the simple FRW cosmological models. In this case η is a function that depends only on t in these models: $\eta = f(t)$.

To facilitate comparisons between the numerical cosmological solutions computed in this study and the simple analytical FRW cosmological models it will be helpful to define a scale factor $a(t)$ for the numerical models that measures how the determinant of the spatial metric, $g(t) = \det g_{ij}(t)$, evolves with time:

$$a^6(t) = \frac{g(t)}{g(0)}. \tag{41}$$

The spatial average $\langle\!\langle a(t)\rangle\!\rangle$, defined by

$$\langle\!\langle a(t)\rangle\!\rangle^3 = \frac{\int \sqrt{g(t)}\,d^3x}{\int \sqrt{g(0)}\,d^3x} = \frac{\mathcal{V}(t)}{\mathcal{V}(0)}, \tag{42}$$

can therefore serve as a generalization of the scale factor used in the analytic FRW cosmological models. The spatial variations in $a(t)$ can be measured with respect to its spatial average, $\langle\!\langle a(t)\rangle\!\rangle$, by evaluating the norm $\| \Delta a \|$ defined by

$$\| \Delta a \|^2 = \frac{\int \left[a(t) - \langle\!\langle a(t)\rangle\!\rangle\right]^2 \sqrt{g}\,d^3x}{\langle\!\langle a(t)\rangle\!\rangle^2\,\mathcal{V}(t)}. \tag{43}$$

Similarly the homogeneity of the lapse N can be evaluated:

$$\| \Delta N \|^2 = \frac{\int \left[N(t) - \langle\!\langle N(t)\rangle\!\rangle\right]^2 \sqrt{g}\,d^3x}{\langle\!\langle N(t)\rangle\!\rangle^2\,\mathcal{V}(t)}, \tag{44}$$

where $\langle\!\langle N(t)\rangle\!\rangle$ is defined by,

$$\langle\!\langle N(t)\rangle\!\rangle = \frac{\int N(t)\sqrt{g}\,d^3x}{\mathcal{V}(t)}. \tag{45}$$

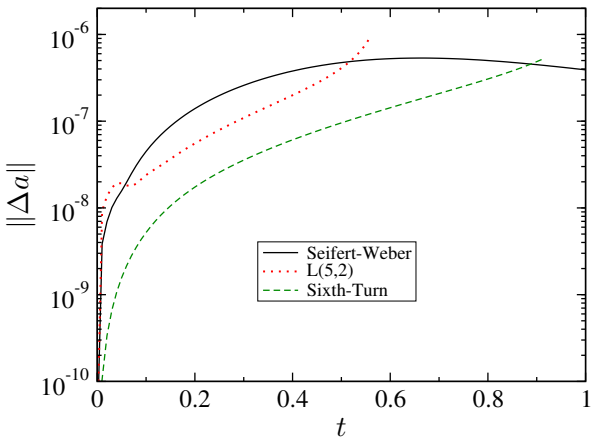


FIG. 14: This figure illustrates the norm $\| \Delta a \|$ defined in Eq. (43) that measures the spatial variations in scale factor $a(t)$ for the $N_{\rm grid} = 28$ solutions to the Einstein evolution equations on the Seifert-Weber, $L(5,2)$, and the Sixth-Turn manifolds.

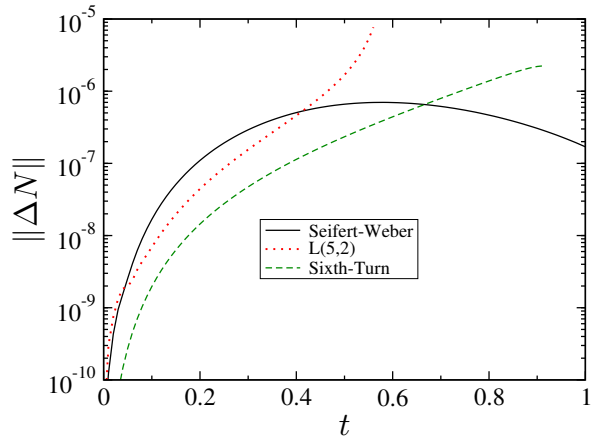


FIG. 15: This figure illustrates the norm $\| \Delta N \|$ defined in Eq. (44) that measures the spatial variations in lapse $N(t)$ for the $N_{\rm grid} = 28$ solutions to the Einstein evolution equations on the Seifert-Weber, $L(5,2)$, and the Sixth-Turn manifolds.

Figures 14 and 15 demonstrate that the scale factor $a(t)$ and the lapse $N(t)$ are essentially constants on each $t =$ constant hypersurface in these numerical evolutions. The spatial variations in the scale factor and the lapse converge toward zero as the spatial resolution $N_{\rm grid}$ increases in all these evolutions. Figures 16 and 17 illustrate these convergence results for the Seifert-Weber and the Sixth-Turn manifolds.

It is interesting to compare the numerical evolution of $\langle\!\langle a(t)\rangle\!\rangle$ with the analogous solutions for $a(\eta)$ from Eqs. (39) and (40). These comparisons are complicated by the fact that the gauge used in the numerical evolutions does not keep the lapse $N(t)$ fixed at its initial value. Consequently the relationship between the numerical time coordinate, t, and the time coordinate, η, used on the FRW cosmological models must be determined

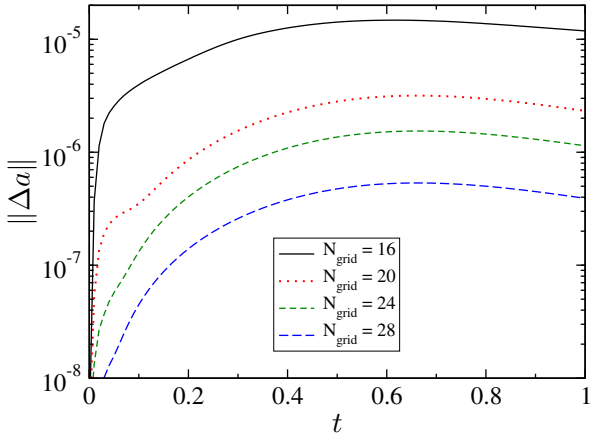


FIG. 16: This figure illustrates the numerical convergence of the norm $\| \Delta a \|$ defined in Eq. (43) as the spatial resolution $N_{\rm grid}$ is increased for solutions to the Einstein evolution equations on the Seifert-Weber manifold.

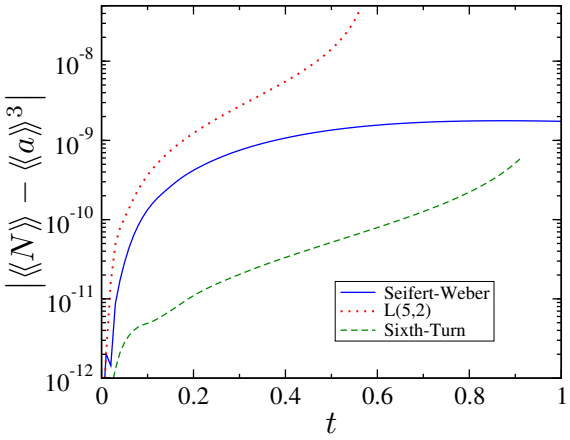


FIG. 18: This figure illustrates the difference between the average value of the Lapse $\langle\langle N(t) \rangle\rangle$ defined in Eq. (36) and the average scale factor $\langle\langle a(t) \rangle\rangle^3$ defined in Eq. (42) for the $N_{\rm grid} = 28$ solution to the Einstein evolution equations on the Seifert-Weber, $L(5,2)$, and the Sixth-Turn manifolds.

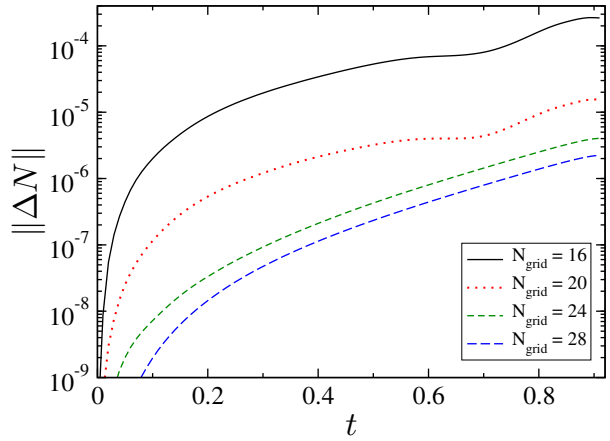


FIG. 17: This figure illustrates the numerical convergence of the norm $\| \Delta N \|$ defined in Eq. (44) as the spatial resolution $N_{\rm grid}$ is increased for solutions to the Einstein evolution equations on the Sixth-Turn manifold.

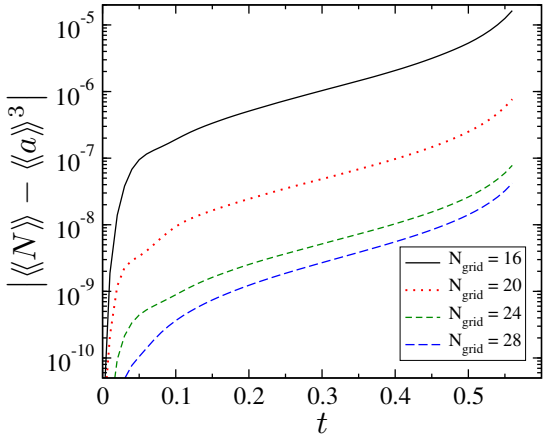


FIG. 19: This figure illustrates the numerical convergence of the difference between the average value of the Lapse $\langle\langle N(t) \rangle\rangle$ defined in Eq. (36) and the average scale factor $\langle\langle a(t) \rangle\rangle^3$ defined in Eq. (42) as the numerical resolution $N_{\rm grid}$ is increased for solutions to the Einstein evolution equations on the $L(5,2)$ manifold.

before comparisons between the cosmological models can be made. Figure 18 shows that the gauge condition that determines that the evolution of the lapse results in the condition $\langle\langle N(t) \rangle\rangle \approx \langle\langle a(t) \rangle\rangle^3$ in these evolutions. Figure 19 illustrates the numerical convergence of this result for the $L(5,2)$ manifold as the spatial resolution $N_{\rm grid}$ increases. Comparing Eq. (36) with Eq. (37) shows that $d\eta/dt = N(t)$. Therefore $d\eta/dt = a^3(t)$, so the FRW version of the Einstein evolution Eqs. (39) and (40) using the time coordinate t used in this study can be written in the forms,

$$\left(\frac{da_{\rm FRW}}{dt} \right)^2 = a_{\rm FRW}^6 \left(-\frac{k}{L^2} + \frac{\Lambda}{3} a_{\rm FRW}^2 \right), \qquad (46)$$

$$\frac{d^2 a_{\rm FRW}}{dt^2} = \frac{3}{a_{\rm FRW}} \left(\frac{da_{\rm FRW}}{dt} \right)^2 + \frac{\Lambda}{3} a_{\rm FRW}^7. \qquad (47)$$

The solutions, $a_{\rm FRW}(t)$, to these FRW cosmology equations can now be compared directly with the $\langle\langle a(t) \rangle\rangle$ for the simple cosmological models computed numerically for this study. In the $k = 0$ case Eq. (46) simplifies to $da_{\rm FRW}/dt = a_{\rm FRW}^4 \sqrt{\Lambda/3}$, which has the analytic solution $a_{\rm FRW}(t) = (1 - \sqrt{3\Lambda}\, t)^{-1/3}$. (This result was also found in Ref. [9] for a numerical cosmological model obtained with the same evolution gauge condition on the non-orientable manifold with spatial topology $P^2 \# P^2 \times S^1$.) In the $k = \pm 1$ cases Eq. (46) does not have simple analytical solutions. In those cases it is more convenient to solve the second-order Eq. (47) numerically. The initial values of $a_{\rm FRW}$ and $da_{\rm FRW}/dt$ at $t = 0$ needed to solve Eq. (47) are fixed by the values of $\langle\langle a(0) \rangle\rangle$ and $d\langle\langle a(0) \rangle\rangle/dt$ from the numerical evolutions at that time. The comparisons

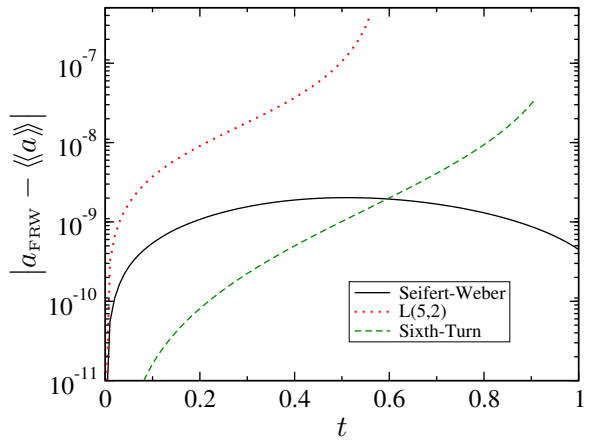


FIG. 20: This figure illustrates the difference between the FRW scale factor $a_{\rm FRW}(t)$ determined by solving Eq. (47) and the average scale factor $\langle\langle a(t)\rangle\rangle$ from the $N_{\rm grid} = 28$ solutions to the Einstein evolution equations on the Seifert-Weber, $L(5,2)$ and the Sixth-Turn manifolds.

between the $a_{\rm FRW}(t)$ computed in this way and $\langle\langle a(t)\rangle\rangle$ are illustrated in Fig. 20 for the three different exemplar manifolds included in this study. These results show that the simple cosmological models computed for this study have the same expansion histories as the standard FRW models within the accuracies of the numerical models.

VI. DISCUSSION

The motivation for this study was to determine whether Ricci flow could be useful in the construction of initial data for realistic cosmological models on manifolds with non-trivial spatial topologies. The results presented here show that convergent numerical solutions to the Ricci flow equation representing homogeneous and isotropic spatial geometries can be constructed successfully on manifolds with a range of topologies. The results of these Ricci flow evolutions were used in this study to prepare initial data for the Einstein evolution equations, which were then solved numerically to construct simple cosmological models. The resulting models were shown to be homogeneous and isotropic, and to have the same expansion histories as the analogous Friedman-Robertson-Walker cosmologies. These results demonstrate the usefulness of Ricci flow in the construction of initial data for realistic cosmological models. The agreement demonstrated here between the complicated numerical results prepared for this study and the analogous results for simple Friedman-Robertson-Walker cosmological models shows the robustness of our numerical methods and their implementation in the `SpEC` code.

The Ricci flow equation is very inefficient to solve numerically because severe limitations on the time step size are required to ensure stable numerical evolutions, see Ref. [27, 28]. A similar problem exists with the numerical solution of elliptic systems of equations like the Einstein initial value equations. In some cases these inefficiency problems have been overcome for the constraint equations by transforming those elliptic systems into damped hyperbolic equations. This hyperbolic relaxation approach has been used successfully in some cases to significantly improve the efficiency of producing numerical solutions to the Einstein constraints, see Refs. [30, 31]. It would be interesting to see whether the parabolic Ricci flow equation could be converted into a damped hyperbolic equation that significantly improves computational efficiency in this case as well.

The harmonic gauge used to produce the numerical evolutions for this study produced cosmological models with $N(t) = a^3(t)$. This results in evolutions in which the scale factor, and therefore the spatial volumes, approaches infinity at finite values of the time parameter. For example in the Sixth-Turn space case $a_{\rm FRW}(t) = (1 - \sqrt{3}\Lambda)^{-1/3}$. This fact severely limits our ability to evolve models numerically long enough to allow the scale factors to increase to the very large values that have been observed in our universe. Therefore it would be very useful to try to develop a gauge condition better suited for these simple cosmological models.

Appendix A: Covariant First-Order Symmetric-Hyperbolic Einstein System

This study uses a covariant representation of the Einstein equations that enforces generalized harmonic gauge conditions, see Ref. [13]. The covariance of this representation is essential for the study of solutions on manifolds with multiple multi-cube coordinate patches, such as the manifolds studied here. All the dynamical fields in this representation are tensors, so they can be transformed in a straightforward way across the interfaces between coordinate patches. The dynamical fields, u^α, for the first-order symmetric-hyperbolic representation of the Einstein equations used in this study are the collection of tensor fields,

$$u^\alpha = \{\psi_{ab}, \Pi_{ab}, \Phi_{iab}\}\,, \tag{A.1}$$

were ψ_{ab} is the spacetime metric, and the tensors Π_{ab} and Φ_{iab} represent its first derivatives,

$$\Pi_{ab} = -t^c \tilde{\nabla}_c \psi_{ab}, \tag{A.2}$$

$$\Phi_{iab} = \tilde{\nabla}_i \psi_{ab}. \tag{A.3}$$

The derivative $\tilde{\nabla}_c$ used in these expressions is the torsion-free covariant derivative compatible with the reference metric $\tilde{\psi}_{ab}$: $\tilde{\nabla}_c \tilde{\psi}_{ab} = 0$. This reference metric is also used to define the Jacobians used to transform tensor fields across the boundary interfaces between multi-cube regions. The vector t^c represents the unit timelike normal ($t^a t^b \psi_{ab} = -1$) to the spacelike hypersurfaces used to perform the evolutions. The lower range of Latin indices, e.g. a, b, c, ..., range over the four spacetime coordinates, while the higher range of indices, e.g. i, j, k, ..., range

over the three spatial coordinates on each t = constant hypersurface. The Greek indices, e.g. α, β, γ, range over the fifty components of the dynamical tensor fields u^α. The Einstein equations for these fields can be written in the first-order form

$$\partial_t u^\alpha + A^{k\alpha}{}_\beta(\mathbf{u})\tilde{\nabla}_k u^\beta = F^\alpha(\mathbf{u}, \tilde{\mathbf{\Gamma}}, \partial\tilde{\mathbf{\Gamma}}), \tag{A.4}$$

where the tensors $A^{k\alpha}{}_\beta(\mathbf{u})$ and $F^\alpha(\mathbf{u}, \tilde{\mathbf{\Gamma}}, \partial\tilde{\mathbf{\Gamma}})$ depend in complicated ways on the dynamical fields u^α, the reference connection $\tilde{\Gamma}^c{}_{ab}$ and its derivatives $\partial_d\tilde{\Gamma}^c{}_{ab}$. The detailed expressions for this representation of the covariant Einstein evolution system are given in Ref. [13].

The spacetime coordinates are determined in the generalized harmonic representations of Einstein's equation by imposing a condition on the difference between the connection $\tilde{\Gamma}^c{}_{ab}$ associated with the reference metric $\tilde{\psi}_{ab}$ and the physical connection $\Gamma^c{}_{ab}$ associated with the physical spacetime metric ψ_{ab}. In particular the difference between these connections is fixed by a gauge source function H_a:

$$H_a = -\psi_{ad}\,\psi^{bc}\left(\Gamma^d{}_{bc} - \tilde{\Gamma}^d{}_{bc}\right). \tag{A.5}$$

(Note that the difference between any two connections is a tensor.) In general H_a may be any function that depends on the physical metric ψ_{ab} (but not its derivatives) and the reference metric $\tilde{\psi}_{ab}$. The gauge condition used for the numerical evolutions performed in this study is the simple harmonic condition, $H_a = 0$.

The generalized harmonic evolution system contains a number of constraints. In particular the gauge condition, Eq. (A.5) is in effect a constraint

$$\mathcal{C}_a = H_a + \psi_{ad}\psi^{bc}\left(\Gamma^d{}_{bc} - \tilde{\Gamma}^d{}_{bc}\right) \tag{A.6}$$

on the dynamical fields. In addition, the equation that defines Φ_{iab}, Eq. (A.3), is also a constraint

$$\mathcal{C}_{iab} = \tilde{\nabla}_i\psi_{ab} - \Phi_{iab}. \tag{A.7}$$

These primary constraints, $\mathcal{C}_a$ and $\mathcal{C}_{iab}$, satisfy a second-order system of evolution equations as a consequence of the Einstein evolution system, Eq. (A.4). (See Ref. [13] for details.) This second-order constraint evolution system can be converted to a first-order symmetric hyperbolic system by introducing the secondary constraints,

$$\mathcal{F}_a = t^c\nabla_c\mathcal{C}_a, \tag{A.8}$$
$$\mathcal{C}_{ia} = \nabla_i\mathcal{C}_a, \tag{A.9}$$
$$\mathcal{C}_{ijab} = 2\tilde{\nabla}_{[i}\mathcal{C}_{j]ab}. \tag{A.10}$$

The symmetric-hyperbolic evolution equation for the collection of constraints,

$$\mathcal{C}^\alpha = \{\mathcal{C}_a, \mathcal{C}_{iab}, \mathcal{F}_a, \mathcal{C}_{ia}, \mathcal{C}_{ijab}\}, \tag{A.11}$$

ensures that solutions to the Einstein Eq. (A.4) that satisfy the constraints, $\mathcal{C}^\alpha$, on an initial surface will satisfy them throughout the evolution of those initial data. Numerical solutions to the equations will of course contain (hopefully small) violations of these constraints. This study monitors the size of these constraint violations by evaluating a norm constructed from the composite constraint, $\mathcal{C}_\psi$, defined by,

$$\begin{aligned}\mathcal{C}_\psi^2 &= \delta^{ab}\left(\mathcal{C}_a\mathcal{C}_b + \mathcal{F}_a\mathcal{F}_b\right)\\ &\quad + \tilde{g}^{ij}\delta^{ab}\delta^{cd}\left(\mathcal{C}_{iac}\mathcal{C}_{jbd} + \tfrac{1}{4}\tilde{g}^{kl}\mathcal{C}_{ikac}\mathcal{C}_{jlbd}\right).\end{aligned} \tag{A.12}$$

This study evaluates a norm of $\mathcal{C}_\psi$, $\|\,\mathcal{C}_\psi\,\|$, defined by

$$\|\,\mathcal{C}_\psi\,\|^2 = \frac{\int \mathcal{C}_\psi^2\sqrt{g}\,d^3x}{\int \mathcal{N}_\psi^2\sqrt{g}\,d^3x}. \tag{A.13}$$

The quantity that appears in the denominator, $\mathcal{N}_\psi$, is defined by

$$\begin{aligned}\mathcal{N}_\psi^2 &= \delta^{ab}\delta^{cd}\tilde{g}^{ij}\left(\partial_i\psi_{ac}\partial_j\psi_{bd} + \partial_i\Pi_{ac}\partial_j\Pi_{bd}\right)\\ &\quad + \delta^{ab}\delta^{cd}\tilde{g}^{ij}\tilde{g}^{kl}\partial_i\Phi_{kac}\partial_j\Phi_{lbd}.\end{aligned} \tag{A.14}$$

It has been included in the definition of $\|\,\mathcal{C}_\psi\,\|$ to provide a dimensionless measure of the fractional errors due to constraint violations in the numerical solutions to the Einstein evolution system.

Acknowledgments

We thank Michael Holst for providing the computational resources used to perform the numerical calculations reported in this study. L.L. was supported in part by grant No. 2407545 from the National Science Foundation to the University of California at San Diego, USA. F.Z. was supported by the National Key Research and Development Program of China grant 2023YFC2205801, and the National Natural Science Foundation of China grants 12433001 and 12021003.

[1] C. J. Copi, D. P. Mihaylov, A. Negro, A. Samandar, G. D. Starkman, Y. Akrami, G. Alestas, S. Anselmi, J. C. Duque, F. Cornet-Gomez, et al. (2026), arXiv:2606.24886.

[2] M. Lachièze-Rey and J.-P. Luminet, Phys. Rep. **254**, 135 (1995).

[3] A. Riazuelo, J. Weeks, J.-P. Uzan, R. Lehoucq, and J.-P. Luminet, Phys. Rev. D **69**, 103518 (2004).

[4] Z.-P. Peng, L. Lindblom, and F. Zhang, J. Cosmology and Astroparticle Physics **12**, 042 (2019).

[5] Planck Collaboration, P. A. R. Ade, N. Aghanim, M. Arnaud, M. Ashdown, J. Aumont, C. Baccigalupi, A. J. Banday, R. B. Barreiro, J. G. Bartlett, et al., Astron. Astrophys. **594**, A13 (2016).

[6] Planck Collaboration, P. A. R. Ade, N. Aghanim, Y. Akrami, P. K. Aluri, M. Arnaud, M. Ashdown, J. Aumont, C. Baccigalupi, A. J. Banday, et al., Astron. Astrophys. **594**, A16 (2016).

[7] R.-G. Cai and S.-J. Wang, Res. in Astron. and Astroph. **26**, 084011 (2026).

[8] N. Secrest, S. von Hausegger, M. Rameez, R. Mohayaee, and S. Sarkar, Rev. Mod. Phys. **97**, 041001 (2025).

[9] F. Zhang and L. Lindblom, Phys. Rev. D **113**, 124012 (2026).

[10] R. S. Hamilton, J. Differential Geom. **17**, 255 (1982).

[11] B. Chow and D. Knopf, *The Ricci Flow: An Introduction*, vol. 110 of *Mathematical Surveys and Monographs* (Amer. Math. Soc., 2004).

[12] L. Lindblom and B. Szilágyi, J. Comput. Phys. **243**, 151 (2013).

[13] L. Lindblom, B. Szilágyi, and N. W. Taylor, Phys. Rev. D **89**, 044044 (2014).

[14] L. Lindblom, N. W. Taylor, and O. Rinne, J. Comput. Phys. **313**, 31 (2016).

[15] L. Lindblom, O. Rinne, and N. W. Taylor, J. Comput. Phys. **460**, 110957 (2022).

[16] F. Zhang and L. Lindblom, Gen. Relativ. Gravit. **54**, 131 (2022).

[17] L. Lindblom and O. Rinne, J. Comput. Phys. **496**, 112579 (2024).

[18] F. Zhang and L. Lindblom, Phys. Rev. D (2026), submitted.

[19] C. Weber and H. Seifert, Mathematische Zeitschrift **37**, 237 (1933).

[20] W. Threlfall and H. Seifert, Math. Ann. **104**, 1 (1931).

[21] J. A. Wolf, *Spaces of Constant Curvature* (AMS Chelsea Publishing, 2011), sixth ed.

[22] P. Scott, Bull. London Math. Soc. **15**, 401 (1983).

[23] D. DeTurck, J. Differential Geom. **18**, 157 (1983).

[24] D. Garfinkle and J. Isenberg, J. Math. Phys. **49**, 073505 (2008).

[25] J. R. Dormand, M. E. A. El-Mikkaway, and P. J. Prince, IMA Journal of Numerical Analysis **7**, 423 (1987).

[26] J. R. Dormand, *Numerical Methods for Differential Equations: A Computational Approach* (CRC Press, Boca Raton, 1996).

[27] C. Canuto, M. Y. Hussaini, A. Quarteroni, and T. A. Zang, *Spectral Methods in Fluid Dynamics* (Springer, 1988).

[28] J. P. Boyd, *Chebyshev and Fourier Spectral Methods* (Dover Publications, 2000).

[29] R. Arnowett, S. Deser, and C. W. Misner, in *Gravitational: An Introduction to Current Research*, edited by L. Witten (Wily, New York, 1962), pp. 227–265.

[30] H. R. Rüter, D. Hilditch, M. Bugner, and B. Brugmann, Phys. Rev. D **98**, 084044 (2018).

[31] F. Zhang and L. Lindblom, Phys. Rev. D **109**, 064002 (2024).